PCCP

Mechanism and Kinetics of the Oxidation of 1,3-Butadien-1-yl (n-C4H5): A Theoretical Study

Journal:	*Physical Chemistry Chemical Physics*
Manuscript ID	CP-ART-02-2021-000567.R1
Article Type:	Paper
Date Submitted by the Author:	31-Mar-2021

Complete List of Authors:	Porfiriev, Denis; Samara University Azyazov, Valeriy; Samara National Research University; Lebedev Physical Institute of RAS, Department of Chemical & Electric Discharge Lasers Mebel, Alexander; Florida International University, Chemistry and Biochemistry

Mechanism and Kinetics of the Oxidation of 1,3-Butadien-1-yl (*n*-C_4H_5): A Theoretical Study

Denis P. Porfiriev,[a] Valeriy N. Azyazov,[b] Alexander M. Mebel,[a,c,*]

[a] *Samara National Research University, Samara 443086, Russian Federation*

[b] *Lebedev Physical Institute, Samara 443011, Russian Federation*

[c] *Department of Chemistry and Biochemistry, Florida International University, Miami, Florida 33199, USA*

Abstract. Ab initio CCSD(T)-F12/cc-pVTZ-f12//B3LYP/6-311G(d,p) calculations of the $C_4H_5O_2$ potential energy surface have been combined with Rice-Ramsperger-Kassel-Marcus Master Equation (RRKM-ME) calculations of temperature- and pressure-dependent rate constants and product branching ratios to unravel the mechanism and kinetics of the *n*-C_4H_5 + O_2 reaction. The results indicate that the reaction is fast, with the total rate constant being in the range of 3.4–5.6×10^{-11} cm^3 $molecule^{-1}$ s^{-1}. The main products include 1-oxo-*n*-butadienyl + O and acrolein + HCO, with their cumulative yield exceeding 90% at temperatures above 1500 K. Two conformers of 1-oxo-*n*-butadienyl + O are formed via a simple mechanism of O_2 addition to the radical site of *n*-C_4H_5 followed by the cleavage of the O-O bond proceeding via a van der Waals C_4H_5O…O complex. Alternatively, the pathways leading to acrolein + HCO involve significant reorganization of the heavy-atom skeleton either via formal migration of one O atom to the opposite end of the molecule or its insertion into the C1-C2 bond. Not counting thermal stabilization of the initial peroxy adducts, which prevails at low temperatures and high pressures, all other products share a minor yield of under 5%. Rate constants for the significant reaction channels have been fitted to modified Arrhenius expressions and are proposed for kinetic modeling of the oxidation of aromatic molecules and 1,3-butadiene. As a secondary reaction, *n*-C_4H_5 + O_2 can be a source for the formation of acrolein observed experimentally in oxidation of the phenyl radical at low combustion temperatures, whereas another significant (secondary) product of the C_6H_5 + O_2 reaction, furan, could be formed through unimolecular decomposition of 1-oxo-*n*-butadienyl. Both the *n*-C_4H_5 + O_2 reaction and unimolecular decomposition of its 1-oxo-*n*-butadienyl primary product are shown not to be a substantial source of ketene.

* E-mail: mebela@fiu.edu

Introduction

In combustion systems, along with oxidation reactions, many alternatives thrive which lead to the production of carcinogenic, mutagenic, and environmentally detrimental species – polycyclic aromatic hydrocarbons (PAHs)[1,2] and soot particles.[3,4] A crucial phase of soot and PAH formation is the origination of the first aromatic cyclic structure that serves as a building block for macromolecules to extend. 1,3-Butadienyl is a species to draw significant attention of combustion chemists because it may serve as a possible intermediate in the formation of the first aromatic ring as well as in the pyrolysis of hydrocarbons and oxyhydrocarbons.[5-10] Two forms of 1,3-butadienyl, *i*-C_4H_5 (2-yl) and *n*-C_4H_5 (1-yl), were carefully investigated theoretically[5,6,11,12] because they can be readily formed by H-abstraction from 1,3-butadiene,[13,14] a ubiquitous combustion intermediate.[15-18] Wheeler et al.[5] inferred, using the focal point method and known thermochemistry for C1-C3 hydrocarbons, that the *n*-isomer lies 10.7 kcal/mol higher in energy than the resonance stabilized *i*-C_4H_5 radical. This result was further corroborated by the quantum Monte Carlo study by Domin et al.[19] Although the rate constant of acetylene addition reaction to *n*-C_4H_5 calculated by Senosiain and Miller[6] is significantly higher than that for *i*-C_4H_5 because of the lower addition barrier, H-assisted isomerization[20] is likely to rapidly convert *n*-C_4H_5 into the more stable *i*-isomer. For this reason, *n*-C_4H_5 was not considered in kinetic models as a significant contributor to the first aromatic ring formation.

Alternatively, the *n*-C_4H_5 isomer may play a notable role in the oxidation of the first aromatic ring, in particular, the phenyl radical, C_6H_5. Venkat et al. predicted that the *n*-butadienyl radical can be formed by the decomposition of 2,4-cyclopentadienone (C_5H_4O).[21] Our recent theoretical calculations have shown however that unimolecular decomposition of 2,4-cyclopentadienone is rather slow and mostly forms the cyclobutadiene + CO products but C_5H_4O can be efficiently consumed via H-assisted decomposition – the C_5H_4O + H reaction, which predominantly produces *n*-C_4H_5 + CO.[22] The same products prevail in the oxidation of the cyclopentadienyl radical with atomic oxygen, C_5H_5 + O. Both cyclopentadienyl (C_5H_5) and 2,4-cyclopentadienone (C_5H_4O) have been inferred to be among the main oxidation products of the phenyl radical via the C_6H_5 + O_2 reaction. While the role of C_5H_5 in the oxidation of the first aromatic ring has been well established,[23] especially at high combustion temperatures,[24] C_5H_4O was detected as a major, likely primary product in a recent study of the C_6H_5 + O_2 reaction in a chemical microreactor at relatively low temperatures of 873 and 1003 K with product identification using photoionization mass spectrometry (PIMS).[25] Several other unexpected products including furan (C_4H_4O), acrolein (C_3H_4O), and ketene (C_2H_2O) were also observed. The authors proposed a reaction mechanism encompassing the primary and secondary reactions in the C_6H_5 + O_2 system and suggested that furan, acrolein, and ketene can be produced through

H-assisted fragmentation of the 1,6-dioxo-3,5-hexadienyl ($C_6H_5O_2$) intermediate. However, kinetic calculations showed that 1,6-dioxo-3,5-hexadienyl is unstable and hence is unlikely to participate in the proposed secondary reaction with H atoms. It is our hypothesis here that the C_4H_4O, C_3H_4O, and C_2H_2O species may be produced instead via oxidation of *n*-C_4H_5, which in turn is the major product of the 2,4-cyclopentadienone + H and cyclopentadienyl + O reactions. Therefore, the goal of the present study is to uncover the mechanism of the *n*-C_4H_5 + O_2 reaction via detailed calculations of the pertinent potential energy surface (PES) and to compute pressure- and temperature-dependent rate constants and product branching ratios. This will help us developing a comprehensive mechanism for the oxidation of C_6H_5, proceeding through a sequence of primary and secondary channels:

$$C_6H_5 + O_2 \rightarrow C_6H_5O + O \rightarrow C_5H_5 + CO + O$$
$$\rightarrow C_5H_4O + HCO$$
$$C_5H_4O + H \,/\, C_5H_5 + O \rightarrow n\text{-}C_4H_5 + CO$$
$$n\text{-}C_4H_5 + O_2 \rightarrow \text{products}$$

In addition to the oxidation of the first aromatic ring, the present study also contributes to the development of an accurate kinetic model for the oxidation of 1,3-butadiene, which is an abundant combustion intermediate and a common pyrolysis product of heavier fuel molecules. The oxidation of the more stable *i*-C_4H_5 isomer has been studied theoretically[12] and the reaction kinetics was recently measured experimentally,[26] but to our best knowledge, *n*-C_4H_5 + O_2 has not been investigated so far and the present work is aimed to fill this gap in knowledge. Since resonantly stabilized radicals like *i*-C_4H_5 tend to react with O_2 slower than regular radicals, the *n*-C_4H_5 + O_2 reaction may significantly contribute to the overall oxidation process of 1,3-butadiene.

Calculation Methods

The PES for the *n*-C_4H_5 + O_2 reaction was mapped out initially via geometry optimization of local minima (reactants, intermediates, and products) and transition states at the density functional B3LYP/6-311G(d,p) level of theory[27,28] using the Gaussian 09 software package.[29] The same approach was utilized in computation of vibrational frequencies and evaluation of zero-point vibrational energy corrections (ZPE). Intrinsic reaction coordinate (IRC) calculations were run to verify stated connections between transition states and local minima. Energies of the majority of predicted species were refined by single-point calculations that employed the explicitly-correlated coupled clusters CCSD(T)-F12 method[30,31] with Dunning's correlation-consistent cc-pVTZ-f12 basis set.[32] Based on T1 diagnostics, two cases of O-eliminations through van der Waals complexes required special multireference treatment, for

which multireference Rayleigh-Schrödinger perturbation theory to the second order, CASPT2,[33] was used. The active space (15,10) in the CASPT2 calculations incorporated all π electrons and the corresponding π and π∗ orbitals as well as all p electrons and p orbitals of the O atoms, along with the electron pair of the O-O bond. The coupled clusters CCSD(T)-F12 and multireference CASPT2 energies were calculated using the Molpro 2010 program package.[34] The expected error of the CCSD(T)-F12/cc-pVTZ-f12//B3LYP/6-311G(d,p) + ZPE(B3LYP/6-311G(d,p)) relative energies lies within 1 kcal/mol according to the assessment by Zhang and Valeev.[35]

The optimized geometries, vibrational frequencies, and relative energies of various species were utilized in Rice-Ramsperger-Kassel-Marcus Master Equation (RRKM-ME) calculations to obtain temperature- and pressure-dependent phenomenological rate constants employing the MESS package.[36,37] All distinct (tight) transition states were handled using conventional transition state theory within the rigid rotor – harmonic oscillator (RRHO) approximation. To deal with the initial barrierless addition of molecular oxygen to *n*-butadienyl we employed phase space theory.[38] We chose the rate constant for the methyl-vinyl + O_2 reaction[39] to fit the high-pressure limit rate constant for the entrance reaction channel of *n*-C_4H_5 + O_2 because of the similarity of the radical structures of H_3C-CHCH (methyl-vinyl) and H_2CCH-CHCH (*n*-C_4H_5). Another barrierless reaction (OH loss from w27 producing furan p3) was tackled using variational transition state theory (VTST).[40] Partition functions of low-frequency torsional modes were treated using 1D or 2D hindered internal rotors, for which the rotational potentials were calculated by a relaxed scan at the B3LYP/6-311G(d,p) level with increments of 30°. Tunneling corrections were included using an asymmetric Eckart approximation. Lennard–Jones parameters for the $C_4H_5O_2$ species, σ = 5.18 Å and ε = 285.2 cm^{-1}, were taken from the study of methyl-vinyl oxidation[39] and for the bath gas N_2, from Jasper et al.'s database, σ = 3.610 Å, ε = 68.0 cm^{-1}.[41] Collisional energy transfer in the master equation was described using the "exponential down" model[42] with energy transfer function parameters n = 0.7 and α_{300} = 333 cm^{-1}.

Results and Discussion

Potential Energy Surface

The PES for the *n*-C_4H_5 + O_2 reaction is very complex and contains 36 intermediates, 83 transition states, and 11 bimolecular products. The overall graph and potential energy diagram of the surface are illustrated in Figures S1 and S2 in Supplementary Information (SI). To simplify the discussion of the PES, it can be divided into two parts. The upper part illustrated in Figure 1 mostly consists of the initial recombination products of *n*-C_4H_5 + O_2 formed in the entrance channel as well as related intermediates that are close in energy, transition state structures

connecting them, and the products of the oxygen atom and OH radical losses from these intermediates, C_4H_5O and C_4H_4O, respectively. The lower part of the PES contains a large variety of intermediates, which are significantly lower in energy than those in the upper part, with their transformations leading towards versatile products. Rearrangements connecting the upper and lower parts of the surface are shown by magenta curves. The corresponding barriers are much lower in the forward direction, towards the lower part of the PES, than in the reverse direction indicating that if the system arrives to this lower part, decomposition to the bimolecular products **p4**-**p9** is much more likely than the return to the upper part of the surface. The O-O bond ruptures in the initial complexes w1 and w2 in the upper part of the PES exhibit barriers that are ~1-5 kcal/mol higher than those for plentiful rearrangements bringing the system to the lower part of the surface and ultimately leading to acrolein, ketene, furan, and furanons. However, the O-atom eliminations are much more preferable from the entropy point of view, at least at higher temperatures. Thus, at a first glance, the reaction outcome should be determined by the competition of the entropy and enthalpy factors, with the former favoring the immediate production of C_4H_5O + O and the latter preferring the other, much more exothermic products.

Although this general conclusion could be made easily, a thorough investigation into the details of the reaction mechanism is truly challenging. Due to the *cis*-*trans* isomerism in *n*-C_4H_5 (**R1** and **R2**), the reaction has two entrance channels respectively leading to the peroxy radicals w1 and w2, which are 44.6 and 44.4 kcal/mol lower in energy than the initial reactants. These adducts can directly decompose by the O-O bond cleavage forming the C_4H_5O products, *trans*- and *cis*-1-oxo-*n*-butadienyl isomers **p1** and **p2** together with atomic oxygen. The corresponding transition states ts1-p1 and ts2-p2 lie lower energy than the products due to the existence of $C_4H_5O\ldots O$ complexes bound by 6.5 and 9.4 kcal/mol. The complexes are not expected to be stable at temperatures relevant to combustion and hence their existence on the PES is not anticipated to affect the overall reaction mechanism and kinetics.

As shown by blue curves in Fig. 1, w1 and w2 can be transformed into one another either directly, by overcoming a barrier at ts1-2 of 29.0 kcal/mol in the w1 → w2 direction and 28.8 kcal/mol in the reverse one, or via dioxy radicals w3 and w4. Various isomerization channels involving the dioxy radicals include one three-step path w1 → ts1-3 → w3 → ts3-4 → w4 → ts2-4 → w2 with the highest barrier of 24.7 kcal/mol and two two-step isomerizations w1→ ts1-4 → w4 → ts2-4 → w2 and w1 → ts1-3 → w3 → ts2-3 → w2 with the highest barriers of 24.7 kcal/mol and 23.1 kcal/mol, respectively. The third possibility involving a shift of the terminal oxygen atom to the neighboring carbon, w1 → ts1-6 → w6, with subsequent conformational change, w6 → ts6-7 → w7, and the final reverse O-shift, w7 → ts2-7 → w2, is the most energetically demanding w1 → w2 isomerization path with the highest barrier of 38.9

kcal/mol relative to w1. Still, this pathway could affect the overall reaction kinetics because of the existence of facile transition from the upper part of the PES to the lower one, w7 → ts7-12 → w12, occurring via the O-O bond rupture achieved by rotation of the terminal HCO group in w7. This step exhibits a very low barrier of 3.3 kcal/mol in the forward direction and a prohibitively high one of 66.9 kcal/mol for the reverse reaction.

Other gateways to the lower part of the PES and the main routes for the formation of acrolein/ketene/furan are insertions of one of the oxygen atoms into the C1-C2 bond through the following reaction steps: w3 → ts3-14 → w14 with the barrier heights of 18.2 and 93.2 kcal/mol in the forward and reverse directions, respectively, and w4 → ts4-13 → w13 (22.3 and 99.6 kcal/mol); a shift of the terminal O-atom in the peroxy group to the hindmost carbon atom: w2 → ts2-21 → w21 (19.6 and 65.1 kcal/mol), five-membered ring closure in w4 → ts4-20 → w20 (25.3 and 75.8 kcal/mol), and a shift of the OH moiety onto the C4 atom in w8 → ts8-24 → w24 (13.1 and 122.0 kcal/mol), where the w8 intermediate itself is produced by 1,5-H migration from the CH_2 group on C4 in w1 to the terminal oxygen on the opposite site of the molecule. The remaining two pathways connecting the upper and lower parts of the PES start from w2 and proceed through the five-membered cyclic structure w5 via two possible ring openings: w2 → ts2-5 → w5 → ts5-22_a/ts5-22_b → w22 and w2 → ts2-5 → w5 → ts5-10 → w10. These transitions possess a common barrier for the first step (19.1 and 15.2 kcal/mol in forward and reverse direction, respectively), whereas the barriers for the second steps differ in heights by 2.3 kcal/mol. The slightly more favorable w5 → w10 isomerization involves opening of the five-membered ring with formation of a three-membered CCO ring in w10. The w5 → w22 rearrangement is more complex and proceeds with the five-membered ring opening followed by a closure of a three-membered CH_2-CH(O)-CH ring and its reopening, as a result of which the CH_2 and CH(O) groups flip their positions in the chain. The energy difference of the transition states ts5-22_a and ts5-22_b is 1.6 kcal/mol.

The upper part of the PES also features two pathways towards furan, which are more demanding energetically in comparison with the channels leading to the lower part of the surface described above. The first route starts from w2 with H-migration from the CH_2 group to the terminal oxygen atom (w2 → ts2-8 → w8) via a 30.8 kcal/mol barrier leading to w8. That structure corresponds to a shallow well with a 9.2 kcal/mol barrier to overcome to form furan + OH via elimination of the hydroxyl group and five-membered ring closure, and an even lower 6.4 kcal/mol barrier back to w2. The second pathway also starts from w2 and involves H shift from C3 to the terminal O atom accompanied with a cleavage of the O-O bond and formation of a van der Waals complex $H_2CCCHCHO\ldots OH$ via a barrier of 27.1 and 47.1 kcal/mol in the forward and reverse direction, respectively, w2 → ts2-9 → w9. The final transformation of w9 to

furan exhibits an even higher barrier of 59.8 kcal/mol because it requires, in addition to the OH loss, 1,2-H shift from CH_2 to the bare C atom prior to the five-membered ring closure. The existence of such a high barrier would likely shift the reaction flux back to w2. Finally, w2 is also connected with the initial *i*-$C_4H_5O_2$ intermediate produced in the *i*-C_4H_5 + O_2 reaction[12] (w2 → w34 → w35, Figure 2) via two consecutive 1,2-H shifts occurring via very high barriers. Since this isomerization is not likely to compete with the other channels described here, the energies for this path were evaluated only at the B3LYP/6-311G(d,p) level of theory.

The lower energy part of the PES can be further dissected into two sections. The first one (see Figure 3 for the potential energy diagram and Figure S3 in SI for the PES graph) consolidates intermediates where one oxygen atom is placed between two carbon atoms. The system can arrive to this part of the surface from the upper PES part via the structures marked by magenta rectangles. Two routes to ketene exist in this area (black curves in Fig. 3). The first one starts from w10 with 1,2-H shift from CHO to CH, w10 → ts10-11_a/ts10-11_b → w11; the difference between the two transition states is that the shifting H atom moves either above or below the C1-C2-C3 plane. This transformation possesses similar high barriers in both directions, 42.8 and 42.1 kcal/mol. The final step is decomposition of w11 via a barrier of 43.1 kcal/mol at ts11-p4 leading to the H_2CCO + c-C_2H_3O products (**p4**) exothermic by 59.4 kcal/mol relative to the *n*-C_4H_5 + O_2 reactants. The second pathway begins with a three-membered CCO ring closure w12 → ts12-15 → w15. Next, the O atom inserts into the C-C bond in the three-membered ring, w15 → ts15-16 → w16. Another 1,2-H shift from the CHO group to the neighboring CH group and subsequent CH_2-O bond cleavage w16 → ts16-17 → w17 → ts17-p5 → **p5** yield ketene plus vinoxy radical (**p5**). Interestingly, the two processes can also take place concertedly in the w16 → ts16-p5 → **p5** single step but in this case 1,3-H migration occurs from CH to CH and the barrier at ts16-p5 is very high, 67.8 kcal/mol. The w16 → ts16-17 → w17 → ts17-p5 → **p5** two-step mechanism features much lower barriers. The outset of the path from w12 to **p5** is characterized by much more symmetric barriers than the end of this route. The well at w15 is shallow and the reverse step back to w12 is slightly energetically more favorable (7.3 kcal/mol) than the forward one to w16 (8.4 kcal/mol), whereas the exit from w16 features barriers of at least 43.5 kcal/mol in the forward direction and more than twice lower, 21.5 kcal/mol, in the reverse direction. Among the counterparts of ketene, c-C_2H_3O **p4** can easily lose an H atom producing a second ketene molecule with the reaction energy being only 0.4 kcal/mol, whereas the vinoxy radical **p5** at combustion temperatures would predominantly decompose to be CH_3 + CO.[43] The H atom loss to form ketene from vinoxy requires 35.1 kcal/mol.

Routes to acrolein (green curves in Fig. 3) and furanone (brown curves) start from the interconnected group of three intermediates w12, w13, w14. Furanone is formed through a six-membered ring closure which could be achieved in two ways, w13 → ts13-18_a/ts13-18_b → w18, leading to the same intermediate w18. The difference in the transition states a and b is that, in the energetically less favorable case b, the ring closure is preceded by the OCH-group rotation. The six-membered ring in w18 then contracts to a five-membered one with an oxygen atom occupying a bridging position on one of the C-C bonds through the w18 → ts18-19 → w19 rearrangement. Next, the bridging O atom takes an out-of-ring position in w20 via a low barrier at ts19-20 and the final step is H elimination, w20 → ts20-p7 → **p7**. The barrier heights on this path are generally lower than for the ketene forming channels. However, all the initial structures in this submechanism (w12, w13, w14) feature energetically comparable but simpler, one-step routes towards acrolein + HCO (**p6**). Moreover, the "magenta" step to w20 from the upper part of the PES (from w4, Fig. 1) possesses the highest barrier among all transitions to the lower part of the surface and hence this intermediate is not easily accessible. w12 decomposes to acrolein + HCO via a barrier of only 3.2 kcal/mol (w12 → ts12-p6 → **p6**) but can also isomerize to w13 (w12 → ts12-13 → w13) and w14 (w12 → ts12-14 → w14) via identical 4.7 kcal/mol barriers. The intermediates w13 and w14 reside in much deeper potential wells than w12 and their one step-decompositions to acrolein + HCO require a C-O bond cleavage (instead of a C-C bond cleavage in w12) and exhibit much higher barriers of 42.2 and 38.6 kcal/mol, respectively. Summarizing, the intermediates w12-w14 are expected to predominantly produce acrolein + HCO (**p6**) rather than **p4**, **p5**, or **p7**.

The remaining part of the PES (Figure 4 and Figure S4 in SI) is the most tangled one. Again, the pivot structures connected with the upper part of the surface are framed in magenta. From the energetic point of view, the preferable entry structures are w21 and w22. They are connected through a significantly asymmetric barrier w21 → ts21-22 → w22 with the heights of 18.2 and 44.7 kcal/mol for the forward and reverse step, respectively. From w22, acrolein could be obtained by detachment of formyl HCO via a barrier of 27.4 kcal/mol, the lowest one among all channels originating from w22. Both w21 and w22 can be transformed into w23 by H migrations to one of the O atoms via the second lowest barrier from w22 and the lowest one from w21. Intermediate w23 represents a group of four different conformers of OHCHCHCHCHO also including w24, w25, and w26. The conformers can transform into each other by rotations of the OCH or HOCH groups. The evolutions of w23-w26 proceed mostly through five-membered ring closures to w27 via barriers of 21.4 and 24.4 kcal/mol in the forward and reverse directions for w23, 33.8 and 24.4 kcal/mol for w24, and 19.2 and 18.8 kcal/mol for w26. An additional pathway to w27 involves a simultaneous hydrogen shift

from the CH_2 group to O in w22 accompanied with the ring closure, w22 → ts22-27 → w27, but the barrier in this case is substantially higher. From w27, furan can be formed by elimination of the hydroxyl group w27 → **p3** occurring without an exit barrier. A more energy demanding alternative leading to furanone involves a 1,4-H-shift from the oxygen atom to carbon, w27 → ts20-27 → w20, with subsequent H-elimination, w20 → ts20-p7 → **p7**. There is also a short cut to furanone from the intermediate w21, w21 → ts20-21 → w20, via rotation of the CH_2O group resulting in a five-membered ring closure. Another pathway from the w23-w26 pool of conformers features a hydrogen migration from CHO forming a CH_2O group on the opposite end in w29. However, this route is expected to be significantly slower due to the higher barriers of 37.1 kcal/mol for w23 → ts23-29 → w29 and of 31.3 kcal/mol for w25 → ts25-29 → w29. Rotation of the OH group connects w29 (-106.5 kcal/mol) with w30 (-106.1 kcal/mol) via a barrier of 2-2.4 kcal/mol. Intermediate w30 features a bent CCO group on the contrary to a nearly linear CCO group in w29. Following a 1,5-H shift from OH simultaneous with the five-membered ring closure, w30 → ts20-30 → w20, this part of the PES connects to the part shown in Fig. 3 and described in the previous paragraph.

One more segment of the PES originates at w22. Two distinct H migrations from terminal OCH groups of 1,2- or 1,3-type form a second CH_2 group and lead to w28 which can decompose producing ketene plus vinoxy through a barrier of 31.2 kcal/mol in w28 → ts28-p5 → **p5** or 3-oxopropyl **p9** by elimination CO group through a barrier of 12.1 kcal/mol in w28 → ts28-p9 → **p9**. Another transformation of w28 is a five-membered ring closure w28 → ts28-31 → w31 with a barrier of 21.3 kcal/mol to overcome. The cyclic structure w31 can decompose to furanone isomeric products **p7** and **p8** via an H atom loss either directly, w31 → ts31-p8 → **p8**, or through a preceding 1,2-H shift step, w31 → ts31-32 → w32 → ts32-p8 → **p8** and w31 → ts31-32 → w32 → ts32-p7 → **p7**. Barriers for all the H-elimination steps are similar, 36.7, 36.9, and 34.7 kcal/mol. Finally, a ring reopening w31 → ts31-33 → w33 with a barrier of 36.5 kcal/mol and subsequent C-O bond cleavage in w33 through a barrier of 27.3 kcal/mol produce ketene plus vynoxy (**p5**).

Summarizing this complex PES, we list the most energetically favorable channels for the formation of various products:

$$n\text{-}C_4H_5 + O_2 \rightarrow w1/w2 \rightarrow \mathbf{p1}/\mathbf{p2} + O \qquad (1)$$

Not considering the entrance barrierless O_2 addition to *n*-butadienyl which is common for all products channels and thus controls the overall reaction rate constant but not product branching ratios, and taking into account that the $C_4H_5O\ldots O$ product complexes should be unstable under combustion conditions, the critical transition states in the channel (1) are positioned at -21.1 and

-20.1 kcal/mol relative to the initial reactants and thus feature ~24 kcal/mol barriers relative to the initial adducts w1/w2.

$$n\text{-}C_4H_5 + O_2 \rightarrow w2 \rightarrow w5 \rightarrow w22 \rightarrow w23\ (\rightarrow w24) \rightarrow w27 \rightarrow \text{furan} + HCO\ (\mathbf{p3}) \quad (2)$$

In this furan formation channel the critical transition states are ts2-5 and ts5-22_a lying 19.1 and 18.3 kcal/mol above w2.

$$n\text{-}C_4H_5 + O_2 \rightarrow w2 \rightarrow w5 \rightarrow w10 \rightarrow w11 \rightarrow \text{ketene} + c\text{-}C_2H_3O\ (\mathbf{p4}) \quad (3)$$

Here, the rate-controlling transition states are ts2-5 and ts5-10, 19.1 and 16.0 kcal/mol higher in energy than w2. Ketene also forms in combination with vinoxy (**p5**):

$$n\text{-}C_4H_5 + O_2 \rightarrow w2 \rightarrow w5 \rightarrow w22 \rightarrow w28 \rightarrow \text{ketene} + C_2H_3O\ (\mathbf{p5}) \quad (4)$$

In addition to ts2-5, this channel is controlled by ts5-22_a and ts5_22_b residing 18.3 and 19.9 kcal/mol above w2, respectively. Acrolein + HCO can be also produced via w22:

$$n\text{-}C_4H_5 + O_2 \rightarrow w2 \rightarrow w5 \rightarrow w22 \rightarrow \text{acrolein} + HCO\ (\mathbf{p6}) \quad (5)$$

This channel is advantageous as compared to channel (4) because ts22-p6 is 10.2 kcal/mol lower than ts22-28_a. An alternative route to **p6** involves w4 and w3:

$$n\text{-}C_4H_5 + O_2 \rightarrow w1/w2 \rightarrow w4 \rightarrow w3 \rightarrow w14\ (\rightarrow w12)\ (\rightarrow w13) \rightarrow \text{acrolein} + HCO\ (\mathbf{p6}) \quad (6)$$

The rate-determining transition states for this route are ts1-4, ts2-4, and ts3-14 respectively lying 24.7, 25.1, and 16.9 kcal/mol higher in energy than w2. Furanone isomers together with an H atom, **p7** and **p8**, can be produced as follows:

$$n\text{-}C_4H_5 + O_2 \rightarrow w1/w2 \rightarrow w4 \rightarrow w3 \rightarrow w14 \rightarrow w13 \rightarrow w18 \rightarrow w19 \rightarrow w20 \rightarrow \mathbf{p7} \quad (7)$$

The channel features the same highest in energy transition states as channel (6) to acrolein, however, is unlikely to compete with the latter since w14 and w13 are more probably decompose to **p6** overcoming lower barriers of 38.6 and 42.2 kcal/mol, respectively, whereas the highest barrier on the route from w14 to **p7** (ts18-19) resides 45.4 kcal/mol above w14. Alternatively, w20 can be formed directly from w4:

$$n\text{-}C_4H_5 + O_2 \rightarrow w1/w2 \rightarrow w4 \rightarrow w20 \rightarrow \mathbf{p7} \quad (8)$$

However, in this case the reaction has to proceed through ts4-20, 25.8 kcal/mol above w2 and 8.9 kcal/mol higher in energy than ts3-14. Finally, a pathway via w22 can form both **p7** and **p8**:

$$n\text{-}C_4H_5 + O_2 \rightarrow w2 \rightarrow w5 \rightarrow w22 \rightarrow w28 \rightarrow w31\ (\rightarrow w32) \rightarrow \mathbf{p7}/\mathbf{p8} \quad (9)$$

Transition states ts2-5, ts5-22_a, and ts5_22_b are highest in energy along this path. Here, direct dissociation of w22 to acrolein + HCO via a barrier of 27.4 kcal/mol is likely to over-compete the multistep route to **p7**/**p8** because ts22-p6 is 10.2 kcal/mol lower than ts22-28_a. Moreover, w28 can also dissociate to 3-oxopropyl + CO **p9**:

$$n\text{-}C_4H_5 + O_2 \rightarrow w2 \rightarrow w5 \rightarrow w22 \rightarrow w28 \rightarrow \text{3-oxopropyl} + CO \ (\mathbf{p9}) \qquad (10)$$

where the barrier at ts28-p9 is only 12.1 kcal/mol, 10.2 kcal/mol lower than the isomerization barrier at ts28-31. Considering the multitude of distinct product channels and various competing reaction pathways, predictions on the outcome of the n-C_4H_5 + O_2 reaction at different temperatures and pressures can only be made after RRKM-ME calculation of phenomenological rate constants and product branching ratios in the subsequent section.

Reaction Kinetics

The calculated PES does not contain especially deep potential wells and therefore, collisional stabilization is not anticipated to significantly affect the overall reaction kinetics at temperatures relevant to combustion. Hence, we mostly address rate constants of bimolecular product formation under combustion conditions (Figure 5). Rate constants plotted in this Figure represent aggregate values combining rates constants of the reactions with O_2 starting from *cis* and *trans n*-butadienyl isomers which are weighted using equilibrium fractions of these isomers at given temperatures. Channel specific rate constants at various pressures and corresponding relative product yields are displayed in Figure 6. We begin with rate constants for interconversion of *cis*- and *trans*-*n*-butadienyls (Fig. 5A). One can see their values to gradually grow with temperature and to modestly decrease with pressure, with the ratios of the rate constants at 0.01 atm and 100 atm being 1.68 at 1000 K and 1.07 at 1650 K. Although these rate constants increase with temperature faster than those for the other product channels, the corresponding branching ratio is below 5 % even at 2500 K indicating that the reaction flux back to the reactants is rather small. The products with the slowest rate constants for their formation including 2(3H)-furanone + H, **p8** (Fig. 5F, dashed lines), ketene + vinoxy, **p5** (Fig. 5G), and 3-oxopropyl + CO, **p9** (Fig. 5H) exhibit similar almost perfect Arrhenius behavior, at least under 1500 K. The rate constants do not exceed 1.86×10^{-15}, 9.89×10^{-15}, and 9.56×10^{-14} cm^3 $molecule^{-1}$ s^{-1}, respectively, and so these products can be considered only as a minute trace with the total branching ratio for all three channels being under 0.4 %. The second cohort of products consists of five-membered heterocyclic structures. Rate constants for the formation of 2(5H)-furanone + H (**p7**) display nearly Arrhenius behavior up to 1250 K where the almost linearly growing trend line bends and reaches a maximum (Fig. 5F). The furan + OH (**p3**) formation curves (Fig. 5E) are of peculiar type in comparison to the others, as the slight maximum at 0.01 atm around 1000 K vanishes at higher pressures and is replaced by a minimum at 1 and 10 atm. At 100 atm, both types of extrema can be seen. Such non-monotonic behavior could be attributed to the complexity of the PES, competition between the multiple channels, and by the presence of the energetically unfavorable pathway w2 → ts2-9 → w9 → ts9-p3 → **p3**, which may contribute

only at highest temperatures. Under combustion conditions both sets of rate constants for the formation of furanone and furan are on the order of 10^{-12} cm^3 molecule^{-1} s^{-1}, with their combined yield falling within the 2–4% range.

The main reaction products are *cis* and *trans* isomers of 1-oxo-*n*-butadienyl formed as a result of an O atom loss, as well as acrolein + HCO, as could be expected from the calculated PES. Rate constants for the formations of cis- and trans-1-oxo-*n*-butadienyl lie in the ranges of $0.8–1.3\times10^{-11}$ and $1.4–1.7\times10^{-11}$ cm^3 molecule^{-1} s^{-1} at 1 atm, respectively. The *trans* isomer wins the competition between these products thanks to a lower barrier for the O loss at ts1-p1 (as compared to ts2-p2) and a smaller set of competitive channels, among which only w1 → ts1-3 → w3 exhibits a lower barrier, with ts1-3 lying 1 kcal/mol below ts1-p1. Although the branching ratio of *cis*-1-oxo-*n*-butadienyl increases with temperature and the difference between the yields of the two isomers diminishes, *trans*-1-oxo-*n*-butadienyl surpasses the *cis* isomer by at least 10 %. The total relative yield of 1-oxo-*n*-butadienyls exceeds 65 % almost under all the investigated conditions except at the highest pressures. Even then, their total yield amounts to more than 75 % starting above 1500 K at 10 at 100 atm. The rate constants for acrolein formation lies mostly within $0.6–1.3\times10^{-11}$ cm^3 molecule^{-1} s^{-1} molecule^{-1} at 1 atm exceeding those for cis-1-oxo-n-butadienyl only at temperatures below 700 K, with the relative yield of acrolein being 14-33 %. The above conclusions concerning the dominant reaction products do not hold at the highest pressures and low temperatures where stabilization in the wells w1 and w2 outperforms some (10 atm) or even all processes leading to bimolecular products (100 atm). However, their contributions rapidly decrease, becoming lower 3 % at 900 K under the 10 atm pressure and 6 % at 1375 K for the 100 atm case.

Being thermally stabilized, the initial adducts w1 and w2 can undergo several transformations discussed above, rate constants for the most preferable of which are shown in Figure 7. Almost in the whole range of parameters used, dissociation to 1-oxo-*n*-butadienyls is the predominant path, whereas dissociation to the initial reactants (solid lines) is the least favorite one. Due to existence of rather straightforward two- or three-step transformations from w2 into acrolein (dotted lines) and furan (dashed-dotted lines) contributions of these channels are comparable with the O-elimination or even greater at lowest pressures.

The *n*-C_4H_5 + O_2 reaction explored here have its key product channels similar to those in the related smaller vinyl + O_2[44] and methylvinyl + O_2[39] systems. These include O-, HCO-, and OH-eliminations, along with stabilization of the initial adducts, which dominates at higher pressures and lower temperatures. However, relative yields of acrolein (HCO loss) and 1-oxo-*n*-butadienyls (O loss) differ from the previous results. For *n*-C_4H_5 + O_2, O-elimination outstrips the other processes almost in the whole range of the conditions considered. Such a difference

stems from a stronger stabilizing electron delocalization in the 1-oxo-*n*-butadienyl products. One can draw three resonance structures for 1-oxo-*n*-butadienyls with the unpaired electron on the oxygen, second or fourth carbon atoms, whereas the electronic structure of the vinoxy C_2H_3O ($C_2H_3 + O_2$) and methyl-vinoxy C_3H_5O (CH_3-$C_2H_3 + O_2$) radicals can be represented by only two resonance structures with the oxygen and the second carbon sharing the unpaired electron. The stronger delocalization makes 1-oxo-*n*-butadienyls more stable, with the O-elimination barrier being more than 10 kcal/mol lower than those for the vinylperoxy and methyl-vinylperoxy radicals.

Secondary decomposition of 1-oxo-n-butadienyls

The proposed mechanism of *n*-$C_4H_5 + O_2$ reaction does not explain significant yields of ketene and furan observed in the experimental study of the $C_6H_5 + O_2$ reaction[25]. In a search of potential reaction pathways toward these products, we explored unimolecular decomposition of 1-oxo-*n*-butadienyls, which are the major primary products of *n*-$C_4H_5 + O_2$. The most energetically favorable part of the C_4H_5O PES is shown in Figure 8 and the corresponding rate constants, which are weighted using the **p2**/**p1** equilibrium constant, are depicted in Figure 9. Furan, which is produced via a five-membered ring closure in **p1** followed by H elimination, is found to be the predominant product even at the highest temperatures, whereas the pathways to ketene are hindered by high barriers for H migrations.

Conclusions

According to the CCSD(T)-F12/pVTZ-f12//B3LYP/6-311G(d,p) calculations of the PES combined with RRKM-ME calculations of rate constants and product branching ratios, the *n*-$C_4H_5 + O_2$ reaction mostly produces 1-oxo-*n*-butadienyl + O and acrolein + HCO, with their cumulative yield exceeding 90% at temperatures above 1500 K. 1-oxo-*n*-butadienyl + O are formed via a simple mechanism of O_2 addition to the radical site followed by the cleavage of the O-O bond proceeding via a van der Waals C_4H_5O…O complex, whereas the pathways leading to acrolein + HCO (**p6**), *n*-$C_4H_5 + O_2$ → w2 → w5 → w22 → **p6** and *n*-$C_4H_5 + O_2$ → w1/w2 → w4 → w3 → w14 (→ w12) (→ w13) → **p6**, feature reorganization of the heavy-atom skeleton either via formal migration of one O atom to the opposite end of the molecule or its insertion into the C1-C2 bond. The other products, excluding thermal stabilization of the initial adducts w1 and w2 prevailing at low temperatures and high pressures, share a minor yield of under 5%. The *n*-$C_4H_5 + O_2$ reaction is predicted to be fast, with the total rate constant ($3.4–5.6\times10^{-11}$ cm^3 $molecule^{-1}$ s^{-1}) being more than an order of magnitude higher than the experimental values recently reported for the *i*-$C_4H_5 + O_2$ reaction.[26] Rate constants for the significant reaction

channels have been fitted to modified Arrhenius expressions (Table 1), which are proposed for kinetic modeling of the oxidation of aromatic molecules and 1,3-butadiene. Another significant product observed in the $C_6H_5 + O_2$ experiment,[25] furan, could be formed through secondary reactions of unimolecular dissociation of 1-oxo-*n*-butadienyls. Above 1000 K, their dissociation rate constant to furan + H (**p3a**) exceeds 10^4 s^{-1}, so that their lifetime would be on the range of 100 μs and rapidly falling below the microsecond scale at higher combustion temperatures. On the other hand, both the primary *n*-$C_4H_5 + O_2$ reaction and secondary decomposition of 1-oxo-*n*-butadienyls are demonstrated to be unlikely to produce ketene. A possibility is that ketene can originate from the *i*-$C_4H_5 + O_2$ reaction where *i*-C_4H_5 may be produced via H-assisted isomerization of *n*-C_4H_5. According to the recent experimental measurements,[26] the total rate constant for *i*-$C_4H_5 + O_2$ is 1.2×10^{-12} cm^3 $molecule^{-1}$ s^{-1} at 1000 K, with ketene + CH_2CHO being one of the two main channels. In the meantime, the rate constant for the production of ketene as a minor (trace) product of the *n*-$C_4H_5 + O_2$ reaction is about 8×10^{-14} cm^3 $molecule^{-1}$ s^{-1} at this temperature, i.e., about an order of magnitude lower. We plan to address this issue along with the development of a comprehensive kinetic model for the oxidation of the first aromatic ring capable of describing all experimentally observed primary and secondary reaction products in a forthcoming publication.

Acknowledgements

This work was supported by the Ministry of Higher Education and Science of the Russian Federation under Grant No. 14.Y26.31.0020 to Samara University and by the US Department of Energy, Basic Energy Sciences, under Grant No. DE-FG02-04ER15570 to Florida International University.

Electronic Supplementary Information Available: Graph of the overall PES for the *n*-$C_4H_5 + O_2$ reaction (Figure S1) and its complete potential energy diagram (Figure S2); graphs of the first (Figure S3) and second (Figure S4) parts of the highly exoergic region of the PES for the *n*-$C_4H_5 + O_2$ reaction; pressure- and temperature-dependent channel specific rate constants and relative yields for various products at 0.1 and 10 atm (Figure S5); input files for RRKM-ME calculations for the $C_4H_5 + O_2$ reaction and secondary unimolecular decomposition of C_4H_5O using the MESS package.

Table 1. Parameters of fitted modified Arrhenius expressions $k = A*T^{\alpha}*\exp(-E_a/RT)$ and $k = A_1*T^{\alpha_1}*\exp(-E_a^1/RT) + A_2*T^{\alpha_2}*\exp(-E_a^2/RT)$ for various reactions in the $C_4H_5O_2$ and C_4H_5O systems. Pre-exponential factors A are in $cm^3\ mol^{-1}\ s^{-1}$ for bimolecular reactions and in s^{-1} for unimolecular reactions, E_a are in cal mol^{-1}.

	p, atm	A_1	α_1	E_a^1	A_2	α_2	E_a^2	T-range, K	%[a]
n-$C_4H_5 + O_2 \rightarrow$ **p1**	0.01	0.13206E+33	-5.4868	15140	0.76603E+16	-0.81699	1728.3	500-2500	0.2
	0.1	0.12730E+33	-5.4823	15128	0.76809E+16	-0.81732	1729.2	500-2500	0.2
	1	0.49615E+33	-5.6540	15602	0.99954E+16	-0.84714	1819.5	500-2500	0.2
	10	0.87587E+40	-7.8541	20320	0.11113E+19	-1.3920	3527.9	500-2500	0.3
	100	0.16992E+33	-5.4059	14715	0.47703E+15	-0.46240	3204.1	500-2500	2.2
n-$C_4H_5 + O_2 \rightarrow$ **p2**	0.01	0.25999E+32	-5.3045	14774	0.24164E+16	-0.70580	1765.2	500-2500	0.3
	0.1	0.13139E+32	-5.2204	14563	0.24295E+16	-0.70694	1765.4	500-2500	0.3
	1	0.30713E+32	-5.3302	14835	0.32378E+16	-0.73946	1870.0	500-2500	0.3
	10	0.15674E+35	-6.1903	16281	0.18778E+18	-1.2078	3390.8	500-2500	0.4
	100	0.72518E+32	-5.3220	14869	0.10916E+15	-0.31364	3111.2	500-2500	2.1
n-$C_4H_5 + O_2 \rightarrow$ acrolein + HCO	0.01	0.29048E+29	-4.5677	10275	0.20932E+15	-0.57742	-179.24	900-2500	0.6
	0.1	0.61297E+20	-2.0396	3609.6				700-2500	1.7
	1	0.69699E+20	-2.0552	3649.1				700-2500	1.5
	10	0.46322E+21	-2.2807	4345.5				600-2500	1.3
	100	0.19234E+51	-10.758	26798	0.35402E+23	-2.7448	8185.4	500-2500	4.4
		0.39279E+56	-12.285	27761	0.11042E+79	-20.356	26454	500-1000	0.8
		0.39491E+33	-5.5873	14408				1000-1375	0.05
		0.94073E+50	-10.311	30456				1375-1800	2.0
		0.50196E+17	-1.2224	53.914				1800-2500	0.1
n-$C_4H_5 + O_2 \rightarrow$ furan + OH	0.01	0.57770E+162	-41.122	0.14218E+06	0.62514E+14	-0.51900	2571.9	900-2500	6.3
		0.11854E+26	-3.7805	9361.9				900-1250	4.7
		0.64195E+18	-1.6029	6331.5				1250-2500	0.6
	0.1	0.16084E+22	-2.4680	11609	0.22519E+50	-11.401	17163	800-2500	1.2
	1	0.29432E+17	-1.4545	2175.2	0.31760E+40	-7.1907	39990	800-2500	0.5

	10	0.18845E+18	-1.6837	2688.1	0.23804E-21	9.5533	-10885	700-1650	0.6
		0.52194E-02	3.7954	-12212				1650-2500	1.0
	100	0.99675E+27	-4.3527	11378	0.43991E+09	-1.2021	-14477	600-1375	0.3
		0.14513E+45	-9.0101	27382				1375-1800	2.2
		0.24171E-08	5.3605	-22052				1800-2500	0.4
n-C_4H_5 + O_2 → ketene (**p4**/**p5** combined)	0.01	0.51108E+12	-0.28900	1885.2				600-2500	2.4
		0.12480E+20	-2.4136	9601.6	0.46601E+12	-0.35434	1303.9	600-1500	0.1
		0.14861E+12	-0.15099	1160.5				1500-2500	0.3
	0.1	0.47857E+12	-0.28104	1866.2				600-2500	2.5
		0.56475E+19	-2.3187	9190.8	0.30255E+12	-0.30370	1182.9	600-1500	0.1
		0.15440E+12	-0.15524	1185.0				1500-2500	0.3
	1	0.69280E+12	-0.32544	1996.9				600-2500	1.6
		0.37058E+27	-4.5059	16838	0.44814E+13	-0.60438	2081.6	600-1500	0.2
		0.15420E+12	-0.15496	1191.1				1500-2500	0.3
	10	0.72622E+14	-0.87771	3785.7				600-2500	2.3
		0.16536E+18	-1.9633	5445.0	0.96677E+11	-0.10734	2742.2	600-1500	0.3
		0.18671E+12	-0.17655	1308.0				1500-2500	0.3
	100	0.45600E+23	-3.2276	13299				700-2500	5.5
		0.90977E+34	-6.5054	20225	0.22221E-16	7.9015	-9729.5	700-1500	0.6
		0.95338E+14	-0.88774	4700.6				1500-2500	0.6
p1/**p2** → furan + H	0.01	0.10688E+84	-21.474	69572	0.97546E+38	-8.2623	44260	500-1375	0.5
	0.1	0.63997E+56	-13.015	57993	0.18392E+35	-7.4631	40349	500-1650	4.4
		0.30206E+40	-8.2439	48713	0.89793E+08	0.36221	28708	500-1000	0.3
		0.63857E+53	-12.161	55821				1000-1375	0.1
		0.68844E+74	-18.043	71963				1250-1650	2.3
	1	0.56540E+22	-2.8316	41065	0.31469E-01	2.7784	22546	500-1000	0.3
		0.49353E+45	-9.5117	54324				1000-1800	1.2
	10	0.11954E+36	-6.5558	50747	0.97539E+130	-37.036	77840	500-2000	5.1
		0.40698E+132	-37.379	79295	0.86896E+116	-30.589	91361	500-900	0.05
		0.48574E+40	-7.9040	54857	0.75787E+13	-0.32695	36016	900-1375	0.02
		0.66430E+40	-7.8687	54615				1375-2000	0.3

	100	0.36816E+90	-23.438	71917	0.31916E+22	-10.453	-4026.3	500-800	0.06
		0.20570E+28	-4.1715	48788				800-1500	0.6
		0.36401E+40	-7.5311	59577				1500-2500	2.7

[a]Maximal percentage deviation of the fitted values from the computed rate constants.

Figure Captions

Figure 1. Upper part of the potential energy diagram for the *n*-C_4H_5 + O_2 reaction. Relative energies calculated at the CCSD(T)-F12/cc-pVTZ-f12//B3LYP/6-311G(d,p) + ZPE(B3LYP/6-311G(d,p)) level of theory are given in kcal/mol.

Figure 2. Connection of the n-C_4H_5 + O_2 and *i*-C_4H_5 + O_2 PES. Relative energies calculated at the CCSD(T)-F12/cc-pVTZ-f12//B3LYP/6-311G(d,p) + ZPE(B3LYP/6-311G(d,p)) level of theory are given in kcal/mol.

Figure 3. The first part of the highly exoergic region of the PES for the *n*-C_4H_5 + O_2 reaction. Relative energies calculated at the CCSD(T)-F12/cc-pVTZ-f12//B3LYP/6-311G(d,p) + ZPE(B3LYP/6-311G(d,p)) level of theory are given in kcal/mol.

Figure 4. The second part of the highly exoergic region of the PES for the *n*-C_4H_5 + O_2 reaction. Relative energies calculated at the CCSD(T)-F12/cc-pVTZ-f12//B3LYP/6-311G(d,p) + ZPE(B3LYP/6-311G(d,p)) level of theory are given in kcal/mol.

Figure 5. Pressure- and temperature-dependent channel specific rate constants for various products. A – interconversion of reactants, B - *trans*-1-oxo-*n*-butadienyl + O (**p1**), C – acrolein + HCO (**p6**), D - *cis*-1-oxo-*n*-butadienyl + O (**p2**), E – furan + OH (**p3**), F – solid lines for 2(5H)-furanone + H (**p7**), dashed lines for 2(3H)-furanone + H (**p8**), G – solid lines for ketene + c-C_2H_3O (**p4**), dashed lines for ketene + vinoxy (**p5**), H – 3-oxopropyl + CO (**p9**). Black line – 0.01 atm, red – 0.1 atm, blue – 1 atm, magenta – 10 atm, green – 100 atm.

Figure 6. Pressure- and temperature-dependent channel specific rate constants and relative yields for various products: hollow blue squares – *trans*-1-oxo-*n*-butadienyl + O (**p1**), solid blue squares – stabilization in w1, hollow red circles – *cis*-1-oxo-*n*-butadienyl + O (**p2**), solid red circles – stabilization in w1, hollow green triangles – acrolein + HCO (**p6**), solid green triangles – 3-oxopropyl + CO (**p9**), magenta stars – interconversion of reactants, navy rhombi – furan + OH (**p3**), cyan plus signs – 2(5H)-furanone + H (**p7**), cyan cross symbols – 2(3H)-furanone + H (**p8**), violet right-pointing triangles – ketene + c-C_2H_3O (**p4**), violet left-pointing triangles – ketene + vinoxy (**p5**). A – 0.01 atm, B – 1 atm, C – 100 atm (plots for 0.1 atm and 10 atm are included in Supplementary Information).

Figure 7. Calculated rate constants for unimolecular decomposition of w1 and w2: Solid lines – back to reactants, dashed lines – dissociation to 1-oxo-*n*-butadienyls, dotted lines – to acrolein, dashed-dotted lines – to furan. Blue, magenta, and green lines correspond to 1, 10, and 100 atm, respectively.

Figure 8. Potential energy diagram for the decomposition of 1-oxo-n-butadienyls. Relative energies calculated at the CCSD(T)-F12/cc-pVTZ-f12//B3LYP/6-311G(d,p) + ZPE(B3LYP/6-311G(d,p)) level of theory are given in kcal/mol.

Figure 9. Pressure- and temperature-dependent channel specific rate constants for the decomposition of 1-oxo-n-butadienyls. Solid and dashed lines depict rate constants for the channels leading to furan + H (p3a) and ketene + vinyl (p5a), respectively. Black, red, blue, magenta, and green lines correspond to pressures of 0.01, 0.1, 1, 10, and 100 atm, respectively.

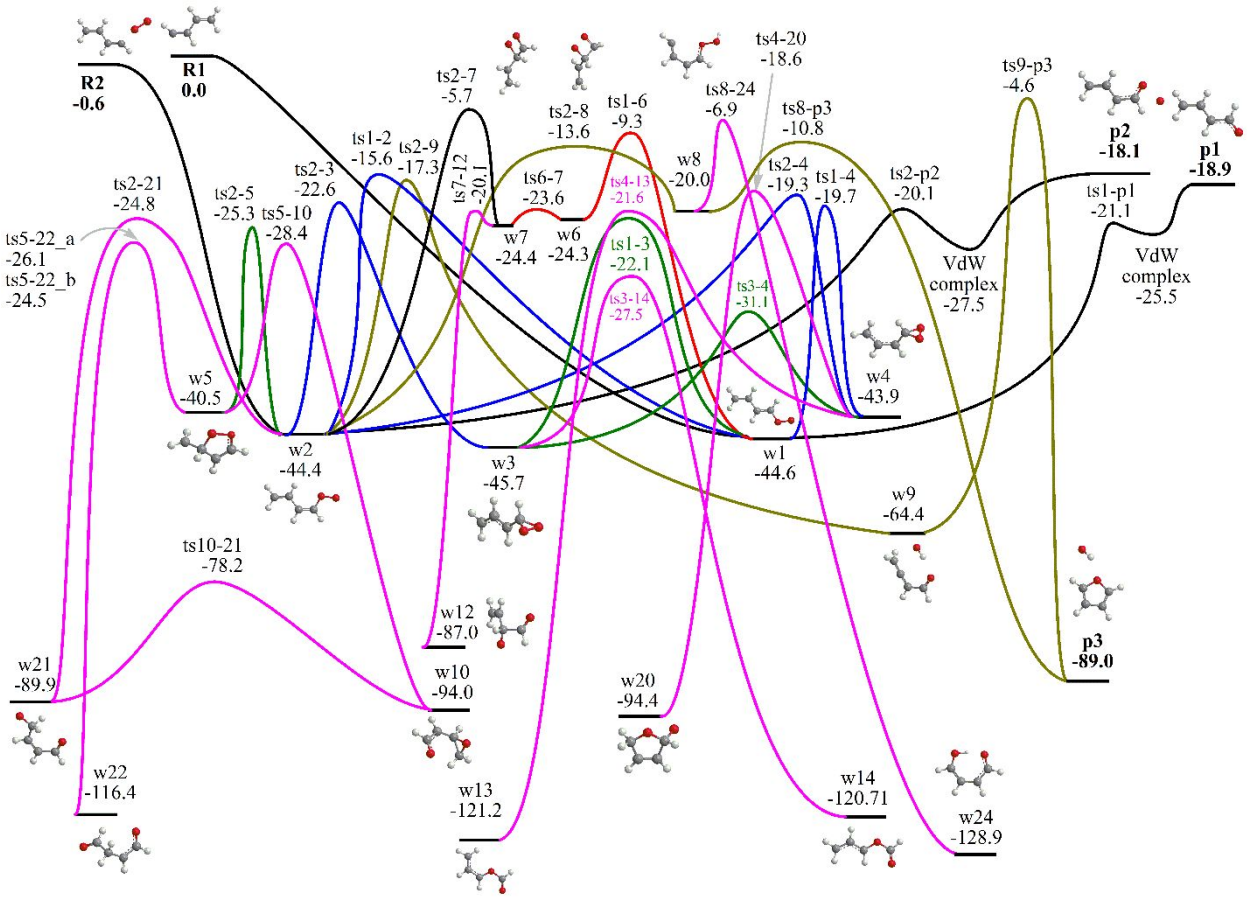

Figure 1. Upper part of the potential energy diagram for the *n*-C_4H_5 + O_2 reaction. Relative energies calculated at the CCSD(T)-F12/cc-pVTZ-f12//B3LYP/6-311G(d,p) + ZPE(B3LYP/6-311G(d,p)) level of theory are given in kcal/mol.

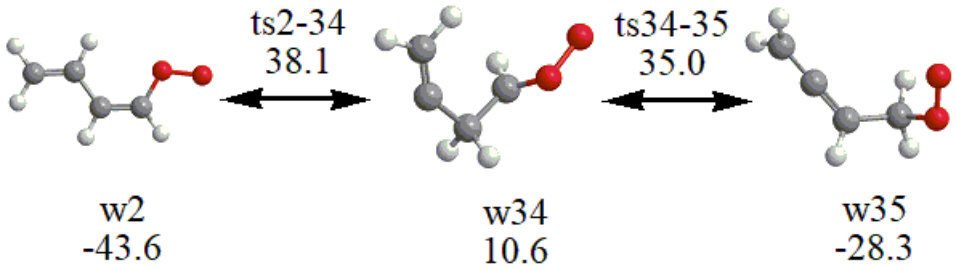

Figure 2. Connection of the n-C_4H_5 + O_2 and *i*-C_4H_5 + O_2 PES. Relative energies calculated at the CCSD(T)-F12/cc-pVTZ-f12//B3LYP/6-311G(d,p) + ZPE(B3LYP/6-311G(d,p)) level of theory are given in kcal/mol.

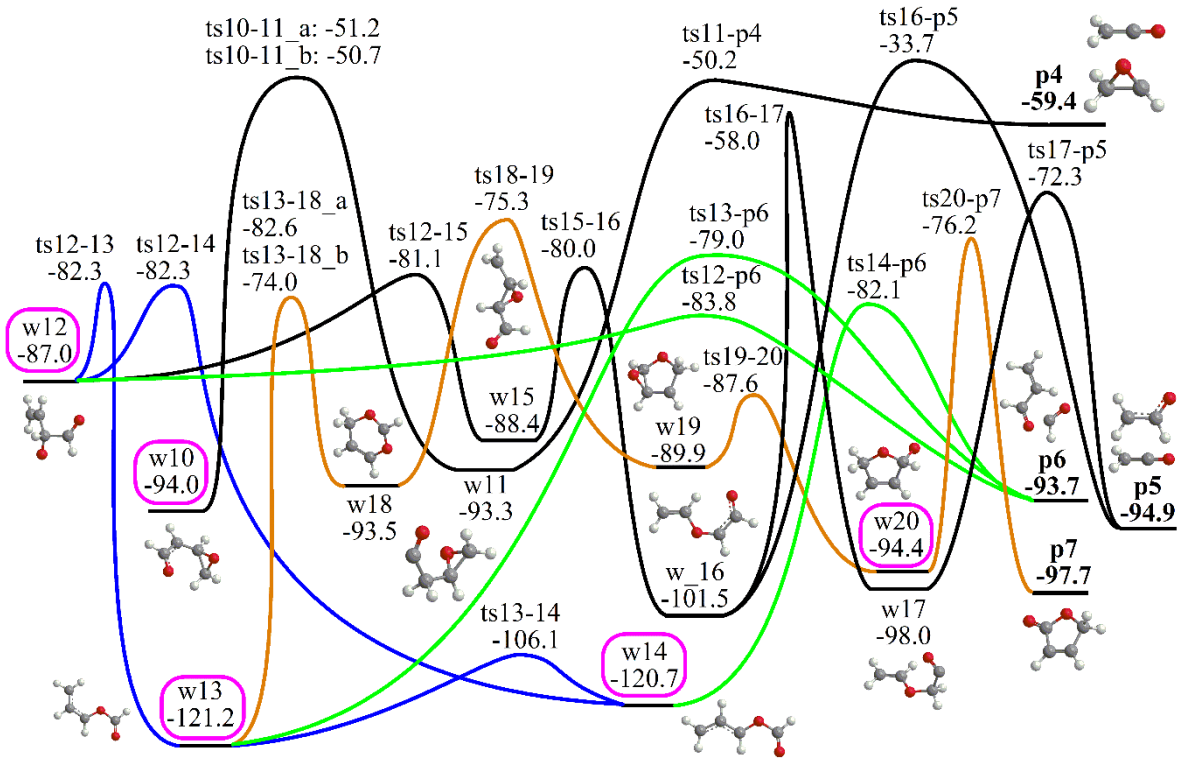

Figure 3. The first part of the highly exoergic region of the PES for the *n*-C_4H_5 + O_2 reaction. Relative energies calculated at the CCSD(T)-F12/cc-pVTZ-f12//B3LYP/6-311G(d,p) + ZPE(B3LYP/6-311G(d,p)) level of theory are given in kcal/mol.

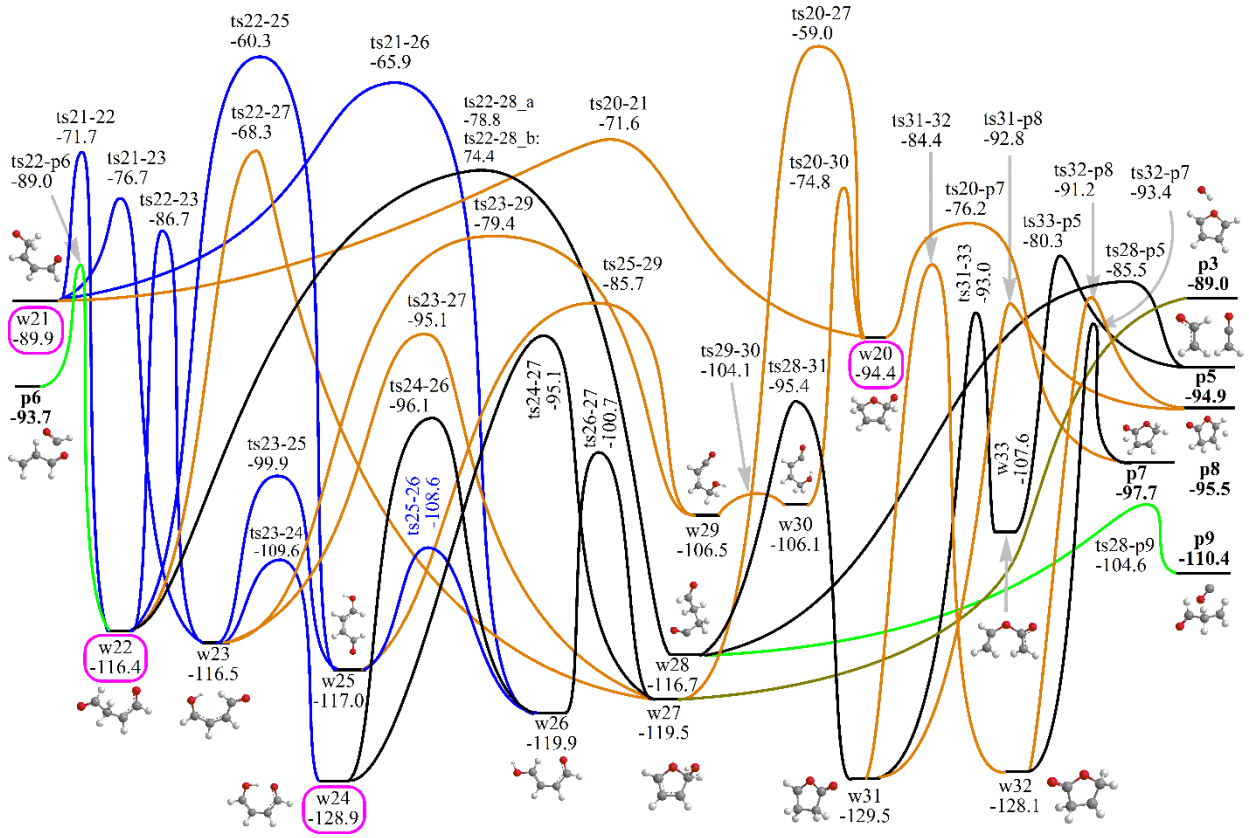

Figure 4. The second part of the highly exoergic region of the PES for the *n*-C_4H_5 + O_2 reaction. Relative energies calculated at the CCSD(T)-F12/cc-pVTZ-f12//B3LYP/6-311G(d,p) + ZPE(B3LYP/6-311G(d,p)) level of theory are given in kcal/mol.

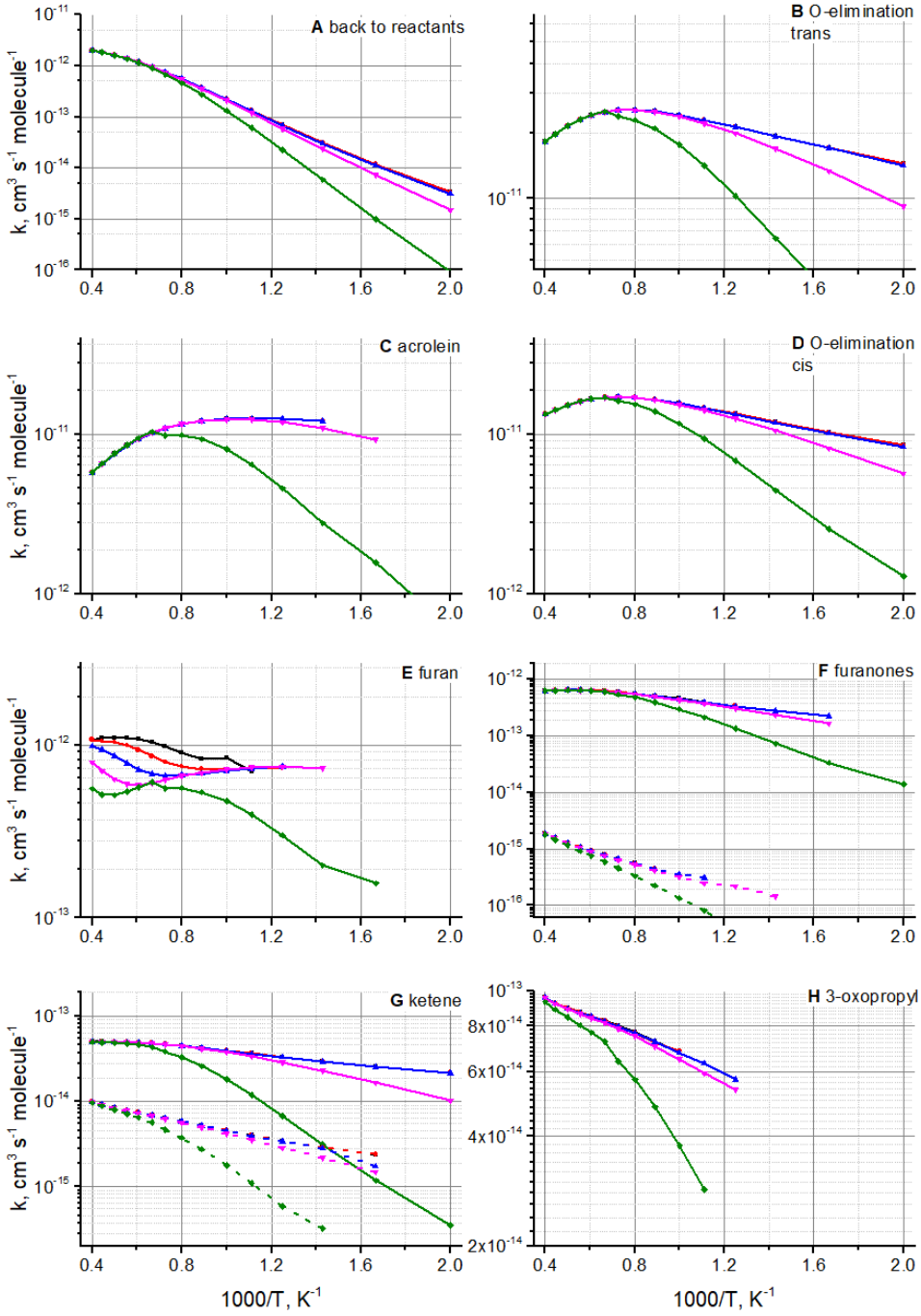

Figure 5. Pressure- and temperature-dependent channel specific rate constants for various products. A – interconversion of reactants, B - *trans*-1-oxo-*n*-butadienyl + O (**p1**), C – acrolein + HCO (**p6**), D - *cis*-1-oxo-*n*-butadienyl + O (**p2**), E – furan + OH (**p3**), F – solid lines for 2(5H)-furanone + H (**p7**), dashed lines for 2(3H)-furanone + H (**p8**), G – solid lines for ketene + c-C_2H_3O (**p4**), dashed lines for ketene + vinoxy (**p5**), H – 3-oxopropyl + CO (**p9**). Black line – 0.01 atm, red – 0.1 atm, blue – 1 atm, magenta – 10 atm, green – 100 atm.

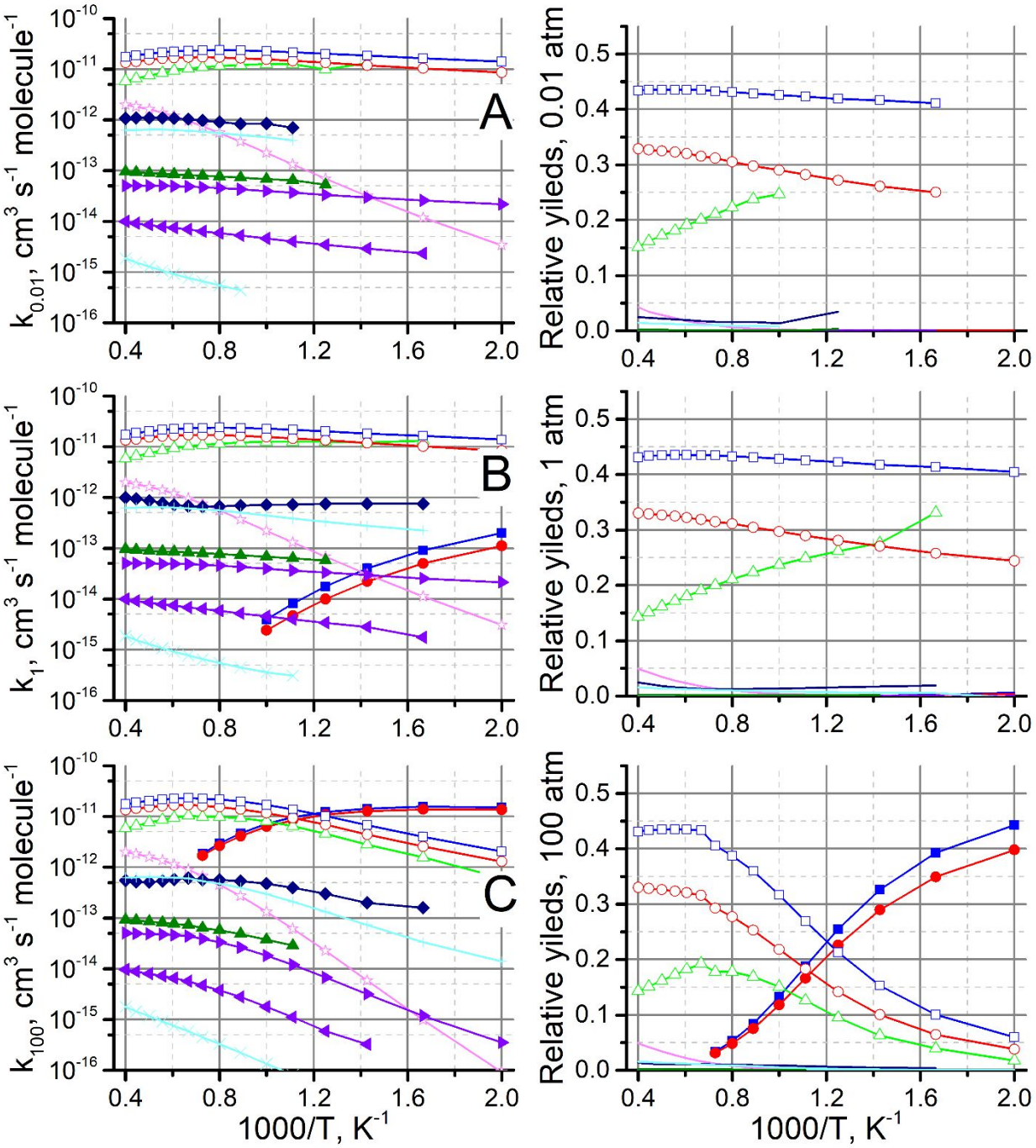

Figure 6. Pressure- and temperature-dependent channel specific rate constants and relative yields for various products: hollow blue squares – *trans*-1-oxo-*n*-butadienyl + O (**p1**), solid blue squares – stabilization in w1, hollow red circles – *cis*-1-oxo-*n*-butadienyl + O (**p2**), solid red circles – stabilization in w1, hollow green triangles – acrolein + HCO (**p6**), solid green triangles – 3-oxopropyl + CO (**p9**), magenta stars – interconversion of reactants, navy rhombi – furan + OH (**p3**), cyan plus signs – 2(5H)-furanone + H (**p7**), cyan cross symbols – 2(3H)-furanone + H (**p8**), violet right-pointing triangles – ketene + c-C_2H_3O (**p4**), violet left-pointing triangles – ketene + vinoxy (**p5**). A – 0.01 atm, B – 1 atm, C – 100 atm (plots for 0.1 atm and 10 atm are included in Supplementary Information).

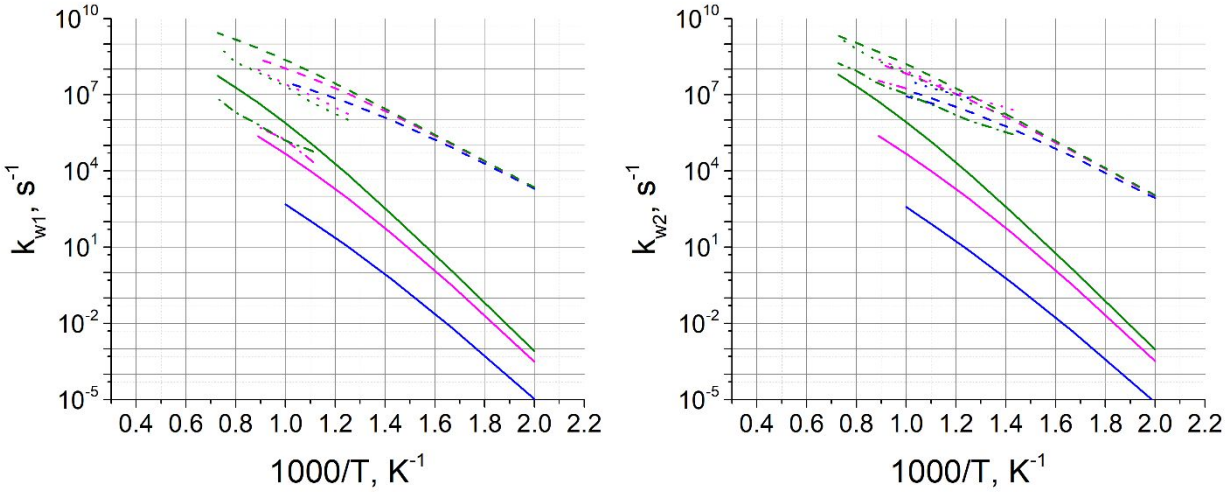

Figure 7. Calculated rate constants for unimolecular decomposition of w1 and w2: Solid lines – back to reactants, dashed lines – dissociation to 1-oxo-*n*-butadienyls, dotted lines – to acrolein, dashed-dotted lines – to furan. Blue, magenta, and green lines correspond to 1, 10, and 100 atm, respectively.

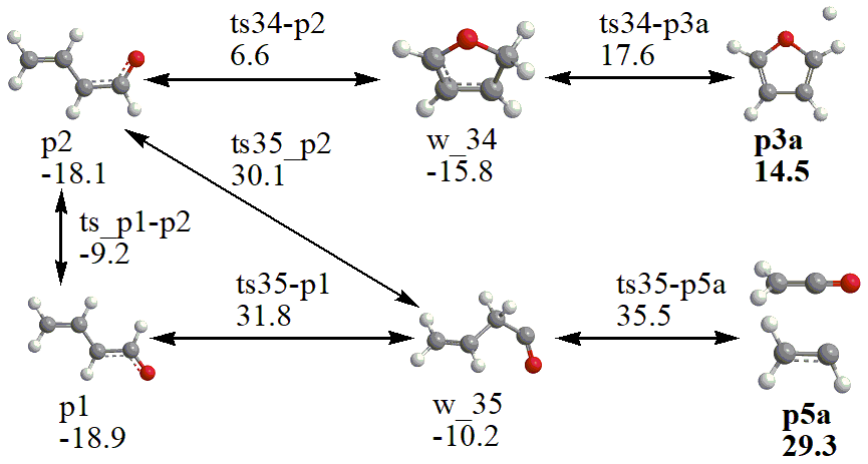

Figure 8. Potential energy diagram for the decomposition of 1-oxo-n-butadienyls. Relative energies calculated at the CCSD(T)-F12/cc-pVTZ-f12//B3LYP/6-311G(d,p) + ZPE(B3LYP/6-311G(d,p)) level of theory are given in kcal/mol.

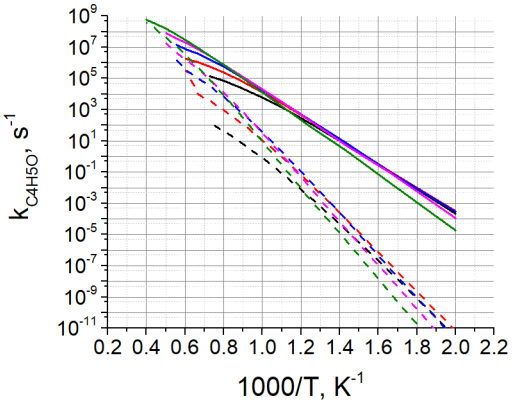

Figure 9. Pressure- and temperature-dependent channel specific rate constants for the decomposition of 1-oxo-n-butadienyls. Solid and dashed lines depict rate constants for the channels leading to furan + H (**p3a**) and ketene + vinyl (**p5a**), respectively. Black, red, blue, magenta, and green lines correspond to pressures of 0.01, 0.1 1, 10, and 100 atm, respectively.

References

1 W. M. Baird, L. A. Hooven and B. Mahadevan, *Environ. Mol. Mutagen.*, 2005, **45**, 106−114.

2 B. J. Finlayson-Pitts and J. N. Pitts Jr., *Science*, 1997, **276**, 1045−1052.

3 M. Frenklach, *Phys. Chem. Chem. Phys.*, 2002, **4**, 2028−2037.

4 H. Richter and J. B. Howard, *Phys. Chem. Chem. Phys.*, 2002, **4**, 2038−2055.

5 S. E. Wheeler, W. D. Allen and H. F. Schaefer, *J. Chem. Phys.*, 2004, **121**, 8800-8813.

6 J. P. Senosiain and J. A. Miller, *J. Phys. Chem. A*, 2007, **111**, 3740-3747.

7 P. M. Winter, M. Rheaume and A. L. Cooksy, *J. Chem. Phys.*, 2017, **147**, 054306.

8 J. A. Miller, M. J. Pilling and J. Troe, *Proc. Combust. Inst.*, 2005, **30,** 43–88.

9 N. Hansen, T. A. Cool, P. R. Westmoreland and K. Kohse-Höinghaus, *Prog. Energy Combust. Sci.*, 2009, **35,** 168–191.

10 C. S. McEnally, L. D. Pfefferle, B. Atakan and K. Kohse-Höinghaus, *Prog. Energy Combust. Sci.*, 2006, **32,** 247–294.

11 N. Hansen, S. J. Klippenstein, C. A. Taatjes, J. A. Miller, J. Wang, T. A. Cool, B. Yang, R. Yang, L. Wei and C. Huang, *J. Phys. Chem. A*, 2006, **110**, 3670–3678.

12 L. K. Rutz, G. da Silva, J. W. Bozzelli and H. Bockhorn, *J. Phys. Chem. A*, 2011, **115**, 1018–1026.

13 S. S. Vasu, J. Zádor, D. F. Davidson, R. K. Hanson, D. M. Golden and J. A. Miller, *J. Phys. Chem. A*, 2010, **114,** 8312–8318.

14 J. Bai, C. Cavallotti and C.-W. Zhou, *Combust. Flame*, 2020, **221**, 228-240.

15 Y. Fenard, G. Dayma, F. Halter, F. Foucher, Z. Serinyel and P. Dagaut, *Energy Fuels*, 2015, **29**, 1107–1118.

16 Y. Zhang, J. Cai, L. Zhao, J. Yang, H. Jin, Z. Cheng, Y. Li, L. Zhang and F. Qi, *Combust. Flame*, 2012, **159**, 905–917.

17 M. Schenk, L. Leon, K. Moshammer, P. Oßwald, T. Zeuch, L. Seidel, F. Mauss and K. Kohse-Höinghaus, *Combust. Flame*, 2013, **160**, 487–503.

18 L. Ruwe, K. Moshammer, N. Hansen and K. Kohse-Höinghaus, *Combust. Flame*, 2017, **175**, 34–46.

19 D. Domin, W. A. Lester Jr., R. Whitesides and M. Frenklach, *J. Phys. Chem. A*, 2008, **112**, 2065-2068.

20 J. A. Miller and C. F. Melius, *Combust. Flame*, 1992, **91,** 21–39.

21 C. Venkat, K. Brezinsky and I. Glassman, *Symp. (Int.) Combust. [Proc.]*, 1982, **19**, 143−152.

22 A. R. Ghildina, A. D. Oleinikov, V. N. Azyazov and A. M. Mebel, *Combust. Flame*, 2017, **183**, 181-193.

23 I. V.Tokmakov, G.-S. Kim, V. V. Kislov, A. M. Mebel and M. C. Lin, *J. Phys. Chem. A*, 2005, **109**, 6114-6127.

24 V. V. Kislov, R. I. Singh, D. E. Edwards, A. M. Mebel and M. Frenklach, *Proc. Combust. Inst.*, 2015, **35**, 1861-1869.

25 D. S. N. Parker, R. I. Kaiser, T. P. Troy, O. Kostko, M. Ahmed and A. M. Mebel, *J. Phys. Chem. A.*, 2015, **119**, 7145-7154.

26 A. J. Eskola, T. T. Reijonen, T. T. Pekkanen, P. Heinonen, S. P. Joshi and R. S. Timonen, *Proc. Combust. Inst.*, 2021, DOI: 10.1016/j.proci.2020.06.031.

27 A. D. Becke, *J. Chem. Phys.*, 1993, **98,** 5648–5652.

28 C. Lee, W. Yang and R.G. Parr, *Phys. Rev. B*, 1988, **37,** 785–789.

29 M. J. Frisch, G. W. Trucks, H. B. Schlegel et al., Gaussian 09, revision B.01, Gaussian, Inc.: Wallingford, CT (2010).

30 T. B. Adler, G. Knizia and H.-J. Werner, *J. Chem. Phys.*, 2007, **127**, 221106.

31 G. Knizia, T. B. Adler and H.-J. Werner, *J. Chem. Phys.*, 2009, **130**, 054104.

32 T. H. Dunning, *J. Chem. Phys.*, 1989, **90**, 1007–1023.

33 P. Celani and H.-J. Werner, *J. Chem. Phys.*, 2000, **112**, 5546.

34 MOLPRO, version 2010.1, a package of ab initio programs, H.-J. Werner, P.J. Knowles, G. Knizia, F.R. Manby, M. Schütz, and others, see http://www.molpro.net.

35 J. Zhang and E. F. Valeev, *J. Chem. Theory Comput.*, 2012, **8**, 3175–3186.

36 Y. Georgievskii and S.J. Klippenstein, Master Equation System Solver (MESS), 2015, available online at https://tcg.cse.anl.gov/papr.

37 Y. Georgievskii, J. A. Miller, M. P. Burke and S. J. Klippenstein, *J. Phys. Chem. A*, 2013, **117**, 12146–12154.

38 S. J. Klippenstein and J. I. Cline, *J. Chem. Phys.*, 1995, **103**, 5451-5460.

39 X. Chen and C. F. Goldsmith, *J. Phys. Chem. A*, 2017, **121**, 9173–9184.

40 J. L. Bao and D. G. Truhlar, *Chem. Soc. Rev.*, 2017, **46**, 7548–7596.

41 A. W. Jasper, J. A. Miller and S. J. Klippenstein, Theoretical Transport, available online at https://tcg.cse.anl.gov/papr/databases/transport.dat.

42 J. Troe, *J. Chem. Phys.*, 1977, **66**, 4745–4757.

43 J. P. Senosiain, S. J. Klippenstein and J. A. Miller, *J. Phys. Chem. A*, 2006, **110**, 5772-5781.

44 C. F. Goldsmith, L. B. Harding, Y. Georgievskii, J. A. Miller and S. J. Klippenstein, *J. Phys. Chem. A*, 2015, **119**, 7766−7779.